https://doi.org/10.1016/j.snb.2017.05.173

Room-temperature polymer-coated supersonic cluster beam deposited ZnO film for O2 gas and dissolved O2 sensing

Man Hon Wong[a] , Ngai Hang Ng[a] , Meng Zhao[b] , Ka Seng Lau[a] , Hau Chung Man[c] , Jeffery T. Cheung[d] and Chung Wo Ong[a], *

a Department of Applied Physics, The Hong Kong Polytechnic University, Hung Hom, Kowloon, Hong Kong, People Republic of China

b Research Center for Solid State Physics and Materials, School of Mathematics and Physics, Suzhou University of Science and Technology, Suzhou 215009, People Republic of China

c Department of Industrial and Systems Engineering, The Hong Kong Polytechnic University, Hung Hom, Kowloon, Hong Kong, People Republic of China

d Department of Physics, Hong Kong Baptist University, Kowloon Tong, Hong Kong, People Republic of China

* Corresponding author. Tel.: +852 27665689; E-mail: c.w.ong@polyu.edu.hk

ABSTRACT

Room-temperature dynamic light-enhanced galvanometric response of supersonic cluster beam deposited (SCBD) zinc oxide (ZnO) films to oxygen (O2) was investigated. The photocurrent was recorded when above bandgap light is turned on, being maintained and turned off. Measurements were done in dry gaseous environment, and repeated in dry and wet gaseous environment after adding a water-proof superhydrophobic polymer coating on top. A dissolved oxygen sensor prototype made of a polymer-coated ZnO film was fabricated to detect oxygen content in water. A model involving photo generation and recombination of electron-hole pairs, trapping and release of conduction electrons associated with sorption-desorption processes of oxygen was proposed. A practical method for

determining the O2 concentration in the media based on fitting parameters to the dynamic photocurrent was tested.

Keywords: Porous ZnO films, UV-assisted photocurrent, O2 sensor, dissolved oxygen detection

1. Introduction

Oxygen (O2) sensing technology has been widely used in many areas such as mining [1], food manufacturing [2], clinical diagnosis [3], environmental monitoring [4] etc. for detecting oxygen in gaseous environment. The technology is also used in aquaculture [5], brewery production [6], wastewater treatment [7, 8], oceanographic research [9, 10] etc. for detecting dissolved oxygen content in liquids. Among various types of oxygen sensors available in the market [11, 12], metal oxide (MOx) gas sensors exhibit distinctive advantages [13-17]. When oxygen molecules approach an MOx, they may capture conduction electrons and be chemisorbed on the oxide surface. A surface depletion layer is formed to increase the sensor's resistance. Upon desorption of oxygen, the sensor's resistance drops as a consequence. This mechanism requires the participation of free electrons. An MOx gas sensor is usually operated at a temperature of a few hundred oC for obtaining a high electron concentration, but the oxide would be annealed progressively to exhibit a drift of the sensor response [18]. Recent development of MOx gas sensors includes two aspects. The first is to use nano MOx materials for making sensors. A nano-structured material has a large surface area. The gas reactions on the oxide surface are enhanced to achieve a stronger sensor response [19-28]. Furthermore, the variation of the volume fraction of the depletion layer relative to the overall nano particle size during loading and unloading is large. The fractional change of the sensor's resistance is more pronounced. In addition, a nano-structured MOx is usually rather porous. The detected gas can diffuse more readily in it to result in a faster response rate. Second, above bandgap light is more often used to illuminate on a direct-bandgap MOx sensor to help in generating electron-hole pairs [29, 30]. The sensor is found to be workable at low temperatures. The problem of thermal instability found in heat-operated MOx gas sensor can be alleviated to 4 some extent. Though some advancements have been achieved, studies of using MOx sensors for detecting dissolved oxygen in a liquid solution are still rarely investigated and reported. In the present study, we started investigated the room-temperature dynamic UV-assisted galvanometric response of porous supersonic cluster beam deposited (SCBD) zinc oxide (ZnO) thin films to oxygen, where the films were post-oxidized at various temperatures from 450 to 600oC. The one post-oxidized at 500oC was selected for detailed study. Measurements were done in dry gaseous environment

containing 0 to 18% O2. After adding a superhydrophobic polymer coating, measurements were repeated in dry and 95% humid gas. An immersion sensor prototype was then fabricated for studying its response to dissolved oxygen in water. A model was proposed to discuss the possible mechanisms involved. A method for determining the dissolved oxygen concentration in water based on the fitting parameters to the dynamic photocurrent was suggested.

2. **Experimental methods**

2.1. Preparation of SCBD ZnO films ZnO films were prepared using SCBD technique. In an SCBD process, a Zn rod of 2 mm in diameter was housed and being rotated in a discharge chamber. 1% O2 balanced in argon (Ar) was pulsed on the target surface at a frequency of 4 Hz. Electric pulses of -900V, with a width of 70 μs and a delay of 650 μs relative to the gas pulses, were applied to the target. Microplasma pulses are ignited to erode the Zn target. Oxidation of sputtered nano Zn particles occurred in the discharge chamber to form ZnO nanoclusters. The nanoclusters were carried by an Ar flow and were deposited on a substrate placed in a high vacuum zone. Single crystal silicon (Si) with (100) plane in parallel with the surface and Corning 7059 glass slides were used as substrates for X-ray 5 diffraction (XRD) experiments and electrical conductivity measurements, respectively. The deposits is a highly porous thin film. Film samples were further post-oxidized at 450, 500, 550 and 600°C, respectively, in an O2 atmosphere for 30 min. They were characterized using a scanning electron microscope (Hitachi SU8010) and an X-ray diffractometer (Rigaku SmartLab). The glancing angle mode was used in XRD experiments, where the incident X-ray beam was set to make an angle of 3o from the substrate surface.

2.2. Galvanometric measurements

Galvanometric response of the films was measured using a home-made system. Details of the system was reported elsewhere [31]. A sample was placed in a stainless steel chamber. Measurements were done at room temperature. A potential of 15 V was applied across two electrodes made on the sample surface. The electrodes were separated by a distance of ≈ 3 mm. A 365-nm and 40-mW ultraviolet (UV) LED was located on the uncoated side of the transparent Corning 7059 glass substrate. Above-bandgap light from the LED passed through the glass substrate and film-substrate interface to shine on the film. Photocurrent was induced when UV was turned on, and extinguished when UV was turned off. The dynamic change of the photocurrent was recorded

using a Keithley 6517A electrometer. Measurements were arranged to have the following parts. (i) The room-temperature dark electrical conductivity of SCBD ZnO film samples post oxidized at 450, 500, 550 and 600°C was measured in vacuum and in dry O2-N2 mixture with the O2 concentration varying from 0 to 18%. One expects to see that the samples have null or very weak response at room temperature. 6 (ii) The room-temperature photoconductivity of SCBD ZnO film samples post-oxidized at above temperatures was measured in vacuum and dry air. One expects to see that UV illumination can generate a photocurrent, and the photocurrent can response to O2 even at room temperature. (iii) A representative film sample was selected based on the results of Part (ii) for more detailed investigation on the photocurrent response to O2. Measurements were done at room temperature with the O2 concentration varying from 0 to 18%. In each measurement, the sample was first set until the dark current became stable. We then turned on the UV light, maintained it for a period and then turned it off. The dynamic change of the photocurrent was recorded throughout the course. (iv) An oxygen-permeable superhydrophobic polymer coating was fabricated on the surface of the selected film sample. The coating was fabricated using a commercial, NeverWet (Rust Oleum Corp.). It comes with two compressed spray bottles. One of them was used first to spray a polypropylene coating on the oxide film. The second one was then used to add a layer of organic solvent (containing acetone, silicones and siloxanes) on top. After being set, the dynamic change of the photocurrent of the film in dry O2-N2 mixture was detected. The O2 concentration was varied from 0 to 18%. (v) The O2-N2 gas mixture was directed to bubble through water in a tank and then admitted into the measurement chamber. The humidity in the measurement chamber was set to become 95%. The dynamic change of the photocurrent in the polymer-coated 500oC annealed SCBD ZnO film was detected again. The O2 was varied over the same range. (vi) An immersion oxygen sensor prototype made of a polymer-coated 500oC-annealed SCBD ZnO film was fabricated. Its structure is presented schematically in Fig. 1. The uncoated side of the glass substrate is attached to the bottom of a plastic bottle where there is a hole. 7 The peripheral in between is sealed. UV light from an LED inside the bottle enters the bare side of the glass substrate and reaches the film/substrate interface. The oxide film was thus illuminated. Fine copper wire feedthroughs are made for completing the circuit. To perform a measurement, the polymer-coated side of the oxide film is immersed into water. The oxygen content in water is set by bubbling O2 or Ar gas into it. The level is read out using a calibrated commercial immersion oxygen detector. UV light is then turned on, maintained for a period and then turned off. One expects that oxygen in water can permeate through the polymer coating and causes some changes of the

dynamic features of the detected photocurrent. The detected changes were associated with the change of dissolved O2 concentration.

3. Results and Discussion

3.1. Film structure of SCBD ZnO films

Figure 2 (a) shows the SEM image of an as-deposited film, and (b) the image taken after 500°C post-oxidization for 1 hour. Nano-sized clusters are in both pictures. One sees that the film remains porous even after the heat treatment. The porosity of the film was estimated by comparing the mass-equivalent thickness measured using a quartz monitor with the actual one measured using a surface profile, which were found to be 21.2 nm and 126 nm, respectively. The porosity was determined to be 83%. After post-oxidation, the film thickness dropped to 85 nm. The porosity reduced slightly to 75%. Fig. 3 shows the XRD spectra of the film samples. One sees that the spectrum of the as deposited film does not show any diffraction peaks associated with metal Zn. Some halos lying around 30-38° are merely seen. This suggests that the film is composed of non-crystalline ZnO clusters. With increasing post-oxidation temperature, the diffraction peaks associated with the 8 (100), (002) (101), (110), (103), (200) and (112) planes of hexagonal phase ZnO became stronger, indicating that the crystallization was enhanced. The linkage between the nanoclusters was also stronger. A small peak at $\approx$ 52o is seen in some spectra. It does not match with any characteristic peaks of Zn and ZnO. An XRD experiment was done on a bare Si(100) substrate using the same glancing angle. We found that when the angle ϕ, a measure of rotation about the axis perpendicular to sample stage, entered a narrow range of a width around $\pm$1.5o , a peak similar to this was seen, but it diminished for ϕ outside this range. It is thereby attributed to the (321) and (311) planes of Si or unknown defects, but not to Zn or ZnO.

3.2. Room-temperature dark conductivity in O2 and photoconductivity in vacuum and air

Fig. 4 (a) shows that the room-temperature dark electrical conductivity of SCBD ZnO films post-oxidized at various temperatures from 450°C to 600°C. It does not show any response to the change of oxygen concentration over a range from 0 to 18% O2 in N2. It also remains unchanged in vacuum after evacuating the measurement chamber. One generally accepted explanation is that surface oxygen sorption occurs, but they are strongly bound to the oxide and are hardly detached. The surface sorbed oxygen concentration and the carrier concentration are not modulated according to the change of surrounding oxygen concentration. The sensor response is very weak or even

undetectable. Surface sorption of this type is referred to as “chemisorption” in literatures. Fig. 4 (b) shows the data of room-temperature photoconductivity, σphoto, of the film samples post-oxidized at 450, 500, 550 and 600°C measured in vacuum. All of the samples showed rather strong photoconductivity. In general, the photocurrent first rises when the UV light is turned on. 9 The increasing rate slows down as time proceeds and the photocurrent approaches towards some level asymptotically. The current extinguishes after the UV light is turned off. The initial response time, asymptotic value and decay time of the current are characteristic parameters of the photocurrent of a sample. Their values vary significantly with post-oxidation temperature. In particular, for the film post-oxidized at low temperature of 450°C, the photocurrent rose by a factor > 105 after a measurement time of 1400 min, and was still increasing until the UV light was turned off. This sample is expected to be less crystallized and has more defects. Electrons could be trapped in the defects. They can transport through hopping or be reexcited to the conduction band. This results in an long effective lifetime for the electrons to contribute to the photocurrent. The response and decay times of the current are comparatively long, and the asymptotic limit is relatively high. On the other hand, samples post-oxidized at higher temperatures are crystallized more significantly and should have less defects. Recombination of the electrons and holes proceeds with a faster rate. Both the response and decay times become shorter, and the asymptotic limit is also lower. Fig. 4 (c) shows the room-temperature photoconductivity σphoto of the samples measured in dry air. In general, its value is much smaller than that detected in vacuum, and the response and decay times are markedly shorter. These observations confirm that above-bandgap light illumination can help to cause changes in the dynamic behavior of the room-temperature photocurrent associated with the change of O2 concentration. Low temperature oxygen detection can thus be realized. This is explained by using a published model [32, 33], which states that when an MOx material is exposed to above-bandgap light, the oxygen species chemisorbed in dark are first desorbed by interacting with photo-generated holes. Oxygen in the environment can also be captured by interacting with photo-generated electrons. They are weakly bound to the 10 oxide and are referred to as the “light-induced surface absorbed” species in this paper. These species are active and readily desorbed from the oxide, such that a high operating temperature as that required by a heat-operated MOx gas sensor is no longer required. In particular, the asymptotic limit of the photocurrent of the 450°C-oxidized film sample in vacuum is 105 times of the dark current and that measured in 18%-O2 is just 200 times of the dark current. This shows that light-induced surface sorption of oxygen suppressed the photocurrent markedly. The films post-oxidized at higher temperatures are less defective and

contain less trap states. The photo generated electrons and holes recombine faster, and hence the suppression of photocurrent by O2 is less significant.

3.3 Oxygen concentration dependence of photoconductivity of 500°C post-oxidized SCBD ZnO film in different measurement environments

After confirming that the films had excellent oxygen sensor response, one further carried out cyclic stability tests on the 450oC- and 500oC-oxidized film samples for identifying which would be more suitable for the use in further investigating the oxygen sensing properties of the material. The tests were done in air. The UV light was turned on and off for ten cycles. Meanwhile, the photocurrent was recorded. Results of the tests are shown in Fig. 5. One sees that the 450oC oxidized sample exhibited stronger photocurrent response, but the signal was less stable. The peak values of the cycles drifted successively to accumulate a total 24% increase after ten cycles, showing a less satisfactory cyclic stability than the other sample. On the contrary, the photocurrent of the 500oC-oxidized film sample only varied by 4% over the test. It was thereby considered to be more stable. Samples oxidized as even higher temperatures showed similar or even slighted improved stability, but the response of the photocurrent dropped continuously. This result is understandable considering that the film structure after going through a higher 11 temperature treatment should be more stable, and hence the gas sensing properties should be more repeatable over the cycles. The reduction of the photocurrent response may be associated with the enhanced crystallization of the material structure. Based on these observations, one believed that the 500oC post-oxidized film exhibited better compromise between the magnitude and stability of O2-induced photocurrent response, and was thereby selected for further oxygen sensing study. Fig. 6 shows the dynamic photocurrent of 500oC-oxidized film sample observed when turning on and off UV light, measured in zero O2 environments (vacuum and nitrogen atmosphere) and in O2-containing environment with the concentration varying from 0.1 to 18%. In zero or low O2 concentration environments, the photocurrent rose first and approached high asymptotic limits. It was not stable yet at the time when the measurements ceased. In higher O2 concentration environments, the photocurrent stabilized much faster. One can identify a saturated photocurrent, Isat in the curves. Its value dropped monotonically with increasing O2 concentration. This is because more oxygen species participate in light-induced surface sorption to reduce the photo generated charge carriers. Further discussion of the relationship between Isat and O2 concentration will be presented in Section 3.4. The relationship would have practical application in quantitative determination of O2 concentration.

Figs. 7 (a) and (b) show the dynamic photocurrent of the 500oC-oxidized SCBD ZnO film coated with a superhydrophobic film, measured in zero O2 environments (vacuum and N2) and in dry O2-N2 gas mixture containing various O2 concentrations, respectively. One clearly sees a systematic drop of the asymptotic limit or Isat with increasing O2 concentration. One asserts that oxygen can permeate through the polymer coating to react with the ZnO film so as to change the photocurrent. The feature of the dynamic photocurrent is thereby useable for determining the ambient O2 concentration. Compared with the results obtained before adding the polymer coating, 12 (i) the asymptotic limit of photocurrent or Isat is smaller by more than 10 times, and (ii) the rising rate of photocurrent is much faster, giving a much shorter response time below 10 min for reaching Isat. We note that NeverWet was sprayed on the ZnO film surface in air. Some oxygen molecules were inevitably enclosed at the interfacial region when the polymer coating was formed. This created an effective oxygen-rich environment on the oxide film. In addition, the presence of the polymer coating slowed down the exchange rate between the surface sorbed oxygen and O2 in the detected gas. These conditions made the oxide film to exhibit a high level of surface sorption of oxygen, such that Isat achieved by the polymer-coated ZnO film is markedly lower than that of the uncoated film. Fig. 8 shows the dynamic photocurrent of the polymer-coated film against O2 concentration of 0.1 to 18% balanced in N2, with the relative humidity of the gas set at 95%. One notices that the time required for reaching Isat is almost the same as that achieved in dry O2-N2 gas, but its value is generally 10 smaller. Isat drops monotonically with increasing O2 concentration, indicating that O2 can penetrate through the polymer film in humid condition. The variation of O2 concentration in humid gas can be detected. In this case, some water molecules would adhere to the polymer film surface and interfere the diffusion of oxygen. This results in a reduction of effective sensing area and weakening of the response of Isat to the change of O2 concentration. Fig. 9 shows the dynamic photocurrent of the immersion sensor prototype against the dissolved oxygen content of 0, 25, 50, 75 and 100% of the solubility in water at 25°C. The solubility is known to be 258 μmol L-1. These settings are equivalent to 0, 0.14, 0.29, 0.43 and 0.58% molar concentration of O2 in gas phase at standard temperature and pressure (Table inset in Fig. 9), which are well below the molar concentration of oxygen in air. One sees in Fig. 9 that 13 after turning on the UV light, the photocurrents measured at various dissolved oxygen concentrations rise along similar tracks. However, after turning off the UV light, the curves drop diversely. The one measured at a higher dissolved oxygen concentration dropped with a faster rate. This confirms that the design of the sensor is possible to be used for detecting the dissolved oxygen concentration in water. We noticed

the necessity of adding the water-proof polymer coating for dissolved oxygen measurements. The left bottom of Fig. 1 shows a picture of a sensor well covered by a polymer film taken after measurements. It remains clear and intact. The right bottom of Fig. 1 is the picture of another sample which is not well protected. When a voltage was applied to across the electrodes, the current density leaking through water was large enough to burn away the oxide film.

3.4. Modeling of oxygen concentration dependence of photoconductivity of SCBD ZnO films and its potential applications

We start from reviewing the early findings of Yamazoe et at. [34]. They carried out a study of a temperature programmed desorption chromatogram analysis over a broad temperature range to observe oxygen desorption from a metal oxide in dark condition. Electron spin resonance was employed to examine the states of the adsorbed species. The change of the electrical conductivity of the oxide was measured concurrently to correlate with the respective desorption processes. Results verified that the adsorbed species at temperature below 150oC are in a singly charged O2 - state. They are specified as chemisorbed species, O2 - (ad). The reaction is described using the formula:

$O2 + e- \rightarrow O2$ (1)

At around 150oC or above, the O2 - (ad) ions are thermally desorbed by interacting with free holes:

$14\ h + + O2 \rightarrow O2(g)$ (2)

Electrons from the desorbed species contribute to a pronounced resistance drop of an MOx. These results explain why a high operation temperature is needed for activating a conventional heat-operated MOx gas sensors. Under above-bandgap light illumination, photoelectron-hole pairs are generated in an MOx:

$hv \rightarrow h+ + e-$ (3)

A large photo-generated charge carrier population is set up at room temperature. The photoelectrons also help to desorb the chemisorbed O2 - (ad) ions [35-37]. On the other hand, oxygen from the detected region can reach the oxide surface and be adsorbed to become weakly bound light-induced surface sorbed O2 -* ions:

$O2 + e- + photon \rightarrow O2 -*$ (4)

These O_2^{-*} ions are at an excited state are more readily desorbed at low temperature:

$$h^+ + O_2^{-*} \rightarrow O_2(g) \qquad (5)$$

We further propose a model for describing the relationship between the dynamic features of the photocurrent and oxygen concentration detected in the study. Let n to be the electron concentration and [O2] to be the oxygen concentration in the detected area. The reaction is:

$$dn = G\,dt - n\,R1\,dt - [O_2]\,n\,R2\,dt \qquad (6)$$

The terms on the right are referred to as photo-generated electron-hole pairs and recombination, and trapping of electrons by surface sorbed O2. G, R1 and R2 are constants. Eq. (6) is integrated to obtain the conduction charge carrier concentration. If nd is the carrier concentration in dark, the overall induced current is:

$$I = (VaA/L)\,e\mu[nd + (G/R)\,[1 - \exp(-Rt)]] = Id + I1\,[1-\exp(-Rt)] \qquad (7)$$

15 Va is the applied voltage across the electrodes, A the cross section area = film thickness $\times$ width of the electrodes, L the length of the measured region and μ the carrier drift mobility.

$R \equiv R1 + [O_2]\cdot R2$.

Eq. (7) is used to fit the curves of dynamic photoconductivity with I1 and R to be adjusted as the fitting parameters. The optmized value of I1, combined with the measured dark current Id, is used to calculate the stabilized saturared current Isat = Id + I1. Furthermore, some relationships between the fitting parameters and oxygen concentration are established. These relationships are found to be useable for quantitative determination of oxygen content in different detected environments. Three examples are presented in the following. The first example is to set up the relationship between Isat derived from the curves in Fig. 6 by applying Eq. (7). A function-type relationship is obtained as shown in Fig. 10 (a). It could be used to read out the O2 concentration in a dry gaseous environment according to the detected Isat value using an uncoated SCBD ZnO film. The second example is the relationship between Isat derived from the curves presented in Fig. 8 by applying Eq. (7). A function-type relationship between Isat and O2 concentration is established as shown in Fig. 10 (b). It is useable for reading out the O2 concentration in a highly humid gasesous environment according to the detected Isat using a polymer-coated SCBD ZnO film. The last example is the

relationship between the decay time obtained from the decaying parts of the curves presented in Fig. 9 observed after UV light is turned off. This relationship is shown in Fig. 10 (c). It can be used to read out the dissolved oxygen content in water at room temperature according to the decay time of a photoconductivity curve. The common advantage of these approaches is being capable of estimating the oxygen concentration in a specific environment according to a fitting parameter derived from part of a dynamic photocurrent response, without the need of waiting for equilibrium.

4. Conclusion

In this study, we investigated the UV-assisted dynamic galvanometric response of SCBD ZnO films, both uncoated and coated with a superhydrophobic polymer film, to O2 concentration in various environments. The measurements carried out in the study include the combinations of (i) uncoated ZnO film in dry O2-N2 gas; (ii) polymer-coated ZnO film in dry O2-N2 gas; (iii) polymer-coated ZnO film in 95% humid O2-N2 gas; and (iv) polymer-coated ZnO immersion sensor in water. In all cases, the dynamic photocurrent illustrates systematic change according to the oxygen content in the detected area. The features of the dynamic photocurrent are explained using a model combining the mechanism of e-h pair generation and recombination, trapping and releasing of conduction electrons by surface-adsorbed oxygen species. Results illustrate the feasibility of using the fitting parameters to the dynamic photocurrent response to determine quantitatively the oxygen content in all of the above detected environments.

Acknowledgements

The work described in this paper is substantially supported by Research Grants Council of the Hong Kong Administrative Region [Project No.: PolyU 5016/08P, account code: B-Q10N; Project No.: 5242/11E, account codes: B-Q26D]; the NSF of China [51502186, 11574227, 11374225]; Innovative Technology Fund [Project No.: ITS/558/09, ZP2U, account code: K.11.27.ZP2U]; and Internal grants of The Hong Kong Polytechnic University [account codes : G-UA7P, G-YBB6, G-YBFU and G-YM42].

References

[1] Y.J. Zhao, Y.B. Wei, Y.F. Li, T.T. Zhang, W.S. Zhao, L. Lv, T.Y. Liu, C. Wang, Application of optical fiber oxygen sensor in coal mines, Progress in Mine Safety Science and Engineering II (2014) 1109-1111.

[2] S. Akbar, P. Dutta, C.H. Lee, High-temperature ceramic gas sensors: A review, Int. J. Appl. Ceram. Tec. 3 (2006) 302-311.

[3] H.A. Smithline, N. Rudnitzky, S. Macomber, F.S.J. Blank, Pulse oximetry using a disposable finger sensor placed on the forehead in hypoxic patients, J. Emerg. Med. 39 (2010) 121-125.

[4] P. Medelius, Sensors for monitoring air quality in earth and space environments, Sensors for Environment, Health and Security: Advanced Materials and Technologies (2009) 431-442.

[5] L.L. Zhao, D.L. Li, D.K. Ma, Q.S. Ding, An portable intelligent measurement instrument for dissolved oxygen in aquaculture, Sensor Lett. 8 (2010) 102-108.

[6] S. Anastasova, M. Milanova, D. Todorovsky, Photoluminiscence response of Ru(II) complex immobilized in SiO2-based matrix to dissolved oxygen in beer, J. Biochem. Biophys. Methods 70 (2008) 1292-1296.

[7] P. Villalobos, C.A. Acevedo, F. Albornoz, E. Sanchez, E. Valdes, R. Galindo, M.E. Young, A BOD monitoring disposable reactor with alginate-entrapped bacteria, Bioprocess Biosyst. Eng. 33 (2010) 961-970.

[8] S. Kara, B. Keskinler, E. Erhan, A novel microbial BOD biosensor developed by the immobilization of P. syringae in micro-cellular polymers, J. Chem. Technol. Biotechnol. 84 (2009) 511-518.

[9] C.M. Clark, K. Hancke, A. Xydes, K. Hall, F. Schreiber, J. Klemme, J. Lehr, M. Moline, Estimation of volumetric oxygen concentration in a marine environment with an autonomous underwater vehicle, J. Field Robot. 30 (2013) 1-16.

[10] B. Edwards, D. Murphy, C. Janzen, N. Larson, Calibration, response, and hysteresis in deep-sea dissolved oxygen measurements, J. Atmos. Ocean. Technol. 27 (2010) 920-931.

[11] V. Aroutiounian, Metal oxide hydrogen, oxygen, and carbon monoxide sensors for hydrogen setups and cells, Int. J. Hydrogen Energy 32 (2007) 1145-1158.

[12] R. Ramamoorthy, P.K. Dutta, S.A. Akbar, Oxygen sensors: Materials, methods, designs and applications, J. Mater. Sci. 38 (2003) 4271-4282.

[13] A. Tiburcio-Silver, A. Sanchez-Juarez, SnO2 : Ga thin films as oxygen gas sensor, Mater. Sci. Eng. B Adv. 110 (2004) 268-271.

[14] F. Chaabouni, M. Abaab, B. Rezig, Metrological characteristics of ZnO oxygen sensor at room temperature, Sens. Actuators B 100 (2004) 200-204.

[15] Q.H. Li, Y.X. Liang, Q. Wan, T.H. Wang, Oxygen sensing characteristics of individual ZnO nanowire transistors, Appl. Phys. Lett. 85 (2004) 6389-6391.

[16] A. Kohli, C.C. Wang, S.A. Akbar, Niobium pentoxide as a lean-range oxygen sensor, Sens. Actuators B 56 (1999) 121-128.

[17] W. Menesklou, H.J. Schreiner, K.H. Hardtl, E. Ivers-Tiffee, High temperature oxygen sensors based on doped SrTiO3, Sens. Actuators B 59 (1999) 184-189.

[18] G. Korotcenkov, B.K. Cho, Instability of metal oxide-based conductometric gas sensors and approaches to stability improvement (short survey), Sens. Actuators B 156 (2011) 527-538.

[19] C.C. Huang, B.D. Pelatt, J.F. Conley, Directed integration of ZnO nanobridge sensors using photolithographically patterned carbonized photoresist, Nanotechnol. 21 (2010) 195307.

[20] M. Tonezzer, R.G. Lacerda, Integrated zinc oxide nanowires/carbon microfiber gas sensors, Sens. Actuators B 150 (2010) 517-522.

[21] O. Lupan, L. Chow, G.Y. Chai, A single ZnO tetrapod-based sensor, Sens. Actuators B 141 (2009) 511-517.

[22] M. Zhao, M.H. Wong, C.W. Ong, Achievement of controlled resistive response of nanogapped palladium film to hydrogen, Appl. Phys. Lett. 107 (2015) 033108.

[23] M. Zhao, M.H. Wong, J.X. Huang, C.W. Ong, Ultrathin percolated WO3 cluster film and its resistive response to H2, J. Alloys Compd. 612 (2014) 163-169.

[24] M. Zhao, J.X. Huang, C.W. Ong, Diffusion-controlled H2 sensors composed of Pd-coated highly porous WO3 nanocluster films, Sens. Actuators B 191 (2014) 711-718.

[25] M. Zhao, J.X. Huang, C.W. Ong, Feasibility of H2 sensors composed of tungsten oxide nanocluster films, Int. J. Hydrogen Energy 38 (2013) 15559-15566.

[26] M. Zhao, J.X. Huang, C.W. Ong, Preparation and structure dependence of H2 sensing properties of palladium-coated tungsten oxide films, Sens. Actuators B 177 (2013) 1062-1070.

[27] M. Zhao, C.W. Ong, Improved H2-sensing performance of nanocluster-based highly porous tungsten oxide films operating at moderate temperature, Sens. Actuators B 174 (2012) 65-73.

[28] M. Zhao, J.X. Huang, C.W. Ong, Room-temperature resistive H2 sensing response of Pd/WO3 nanocluster-based highly porous film, Nanotechnol. 23 (2012) 315503.

[29] Y. Muraoka, N. Takubo, Z. Hiroi, Photoinduced conductivity in tin dioxide thin films, J. Appl. Phys. 105 (2009) 103702.

[30] Q.H. Li, Q. Wan, Y.X. Liang, T.H. Wang, Electronic transport through individual ZnO nanowires, Appl. Phys. Lett. 84 (2004) 4556-4558.

[31] M. Zhao, J.X. Huang, M.H. Wong, Y.M. Tang, C.W. Ong, Versatile computer-controlled system for characterization of gas sensing materials, Rev. Sci. Instrum. 82 (2011) 105001.

[32] M. Cho, I. Park, Recent Trends of Light-enhanced Metal Oxide Gas Sensors: Review, J. Sensor Sci. & Tech. 25 (2016) 103-109.

[33] Q. Geng, Z. He, X. Chen, W. Dai, X. Wang, Gas sensing property of ZnO under visible light irradiation at room temperature, Sens. Actuators B 188 (2013) 293– 297.

[34] N. Yamazoe, J. Fuchigami, M Kishikawa, T. Seiyama, Interactions of tin oxide surface with O2, H2O and H2, Surf. Sci. 86 (1979) 335-344.

[35] X. Li, X. Li, J. Wang, S. Lin, Highly sensitive and selective room-temperature formaldehyde sensors using hollow TiO2 microspheres, Sens. Actuators B 219 (2015) 158-163.

[36] S.W. Fan, A.K. Srivastava, V.P. Dravid, UV-activated room-temperature gas sensing mechanism of polycrystalline ZnO, Appl. Phys. Lett., 95 (2009) 142106.

[37] Y. Chen, X. Li, X. Li, J. Wang, Z. Tang, UV activated hollow ZnO microspheres for selective ethanol sensors at low temperatures, Sens. Actuators B 232 (2016) 158-164.

Figure Captions

Fig. 1 Immersion dissolved oxygen sensor prototype made of 500°C post-oxidized SCBD ZnO film. Left and right bottom: pictures of well and poorly protected immersion sensor taken after measurements in water.

Fig. 2 (a) and (b) SEM images of an SCBD ZnO film captured before and after post-oxidization at 500°C for 30 min. The roughness is 15.0 nm and 13.6 nm in respective cases.

Fig. 3 XRD spectra of SCBD ZnO films recorded before and after post-oxidized at 450, 500, 550 and 600°C.

Fig. 4 (a) Room-temperature dark electrical conductivity of SCBD ZnO films post-oxidized at 450°C to 600°C in 0-18% O2-N2 and vacuum; (b) and (c) room-temperature photoconductivity of the films measured in vacuum and air, respectively.

Fig. 5 Room-temperature cyclic photoconductivity of 450oC- and 500oC-post oxidized SCBD ZnO films measured in air.

Fig. 6 Room-temperature dynamic photoconductivity and photocurrent of a 500°C-oxidized SCBD ZnO film to 0 to 18% O2 in N2 in dry gaseous environment.

Fig. 7 (a) and (b) Room-temperature dynamic photoconductivity and photocurrent of a polymer coated 500°C-oxidized SCBD ZnO film measured in 0 – 18% O2 in dry gaseous environment.

Fig. 8 Room-temperature dynamic photoconductivity and photocurrent of a polymer-coated 500°C-oxidized SCBD ZnO film in 0 – 18% O2 in 95% humid gaseous environment.

Fig. 9 Room-temperature dynamic photoconductivity and photocurrent of a polymer-coated 500°C-oxidized SCBD ZnO film in water with 0 – 100% dissolved oxygen content.

Fig. 10 Three examples of relationships correlating the fitting parameters obtained from the dynamic photocurrent of a 500°C-oxidized SCBD ZnO film and O2 concentration. (a) Isat of an uncoated film versus O2 concentration in dry O2-N2 mixture; (b) Isat of a polymer-coated film versus O2 concentration in 95% humid O2-N2 mixture; and (c) decay time of photocurrent after turning off UV light versus dissolved oxygen content in water.

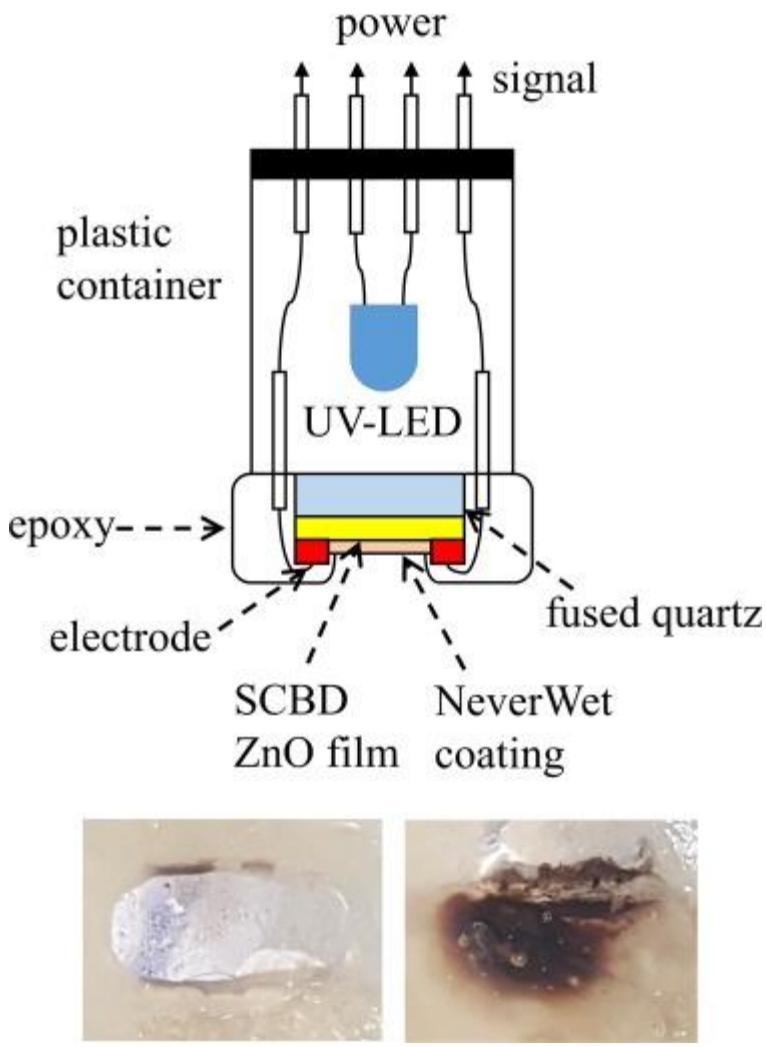

Fig. 1. Immersion dissolved oxygen sensor prototype made of 500 °C post-oxidized SCBD ZnO film. Left and right bottom: pictures of well and poorly protected immersion sensor taken after measurements in water.

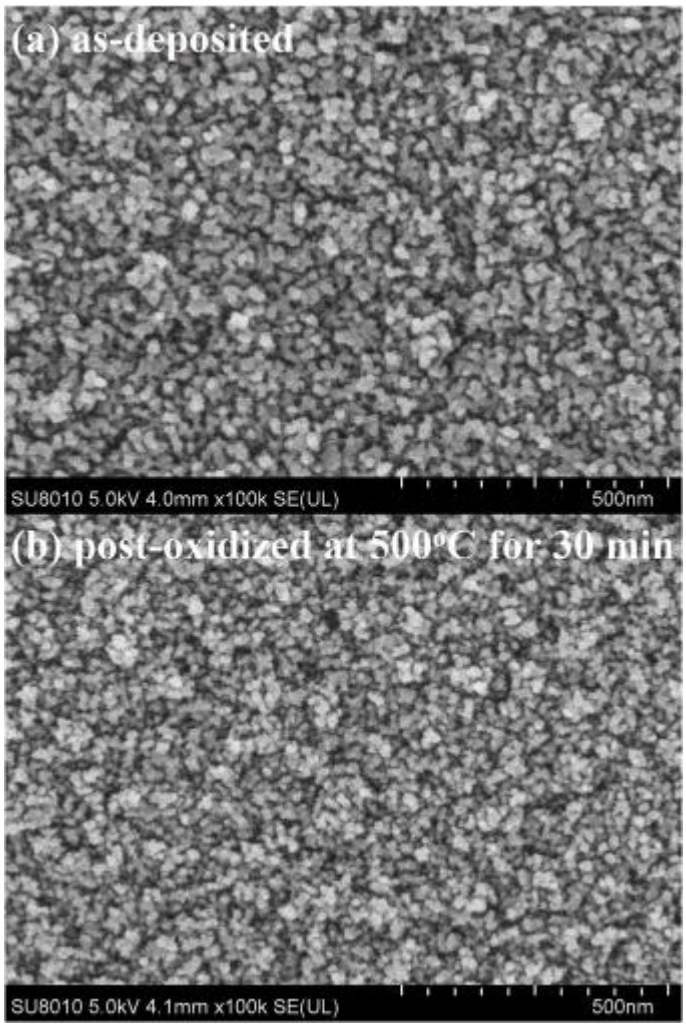

Fig. 2. (a) and (b) SEM images of an SCBD ZnO film captured before and after post-oxidization at 500 °C for 30 min. The roughness is 15.0 nm and 13.6 nm in respective cases.

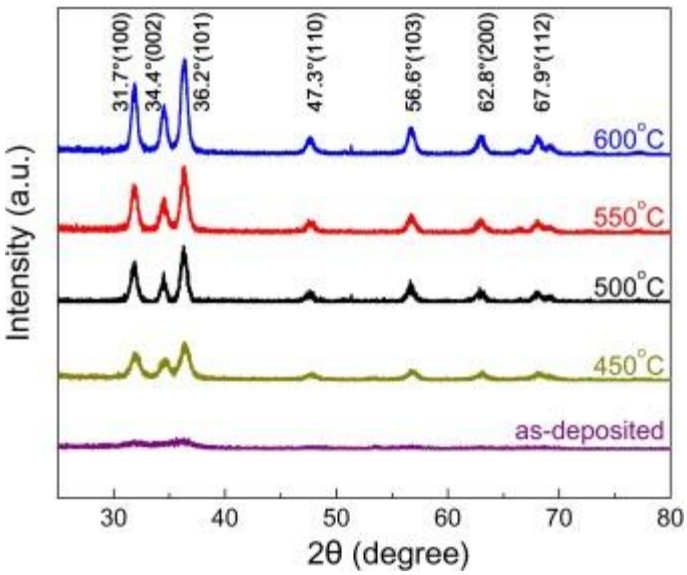

Fig. 3. XRD spectra of SCBD ZnO films recorded before and after post oxidation at 450, 500, 550 and 600 °C.

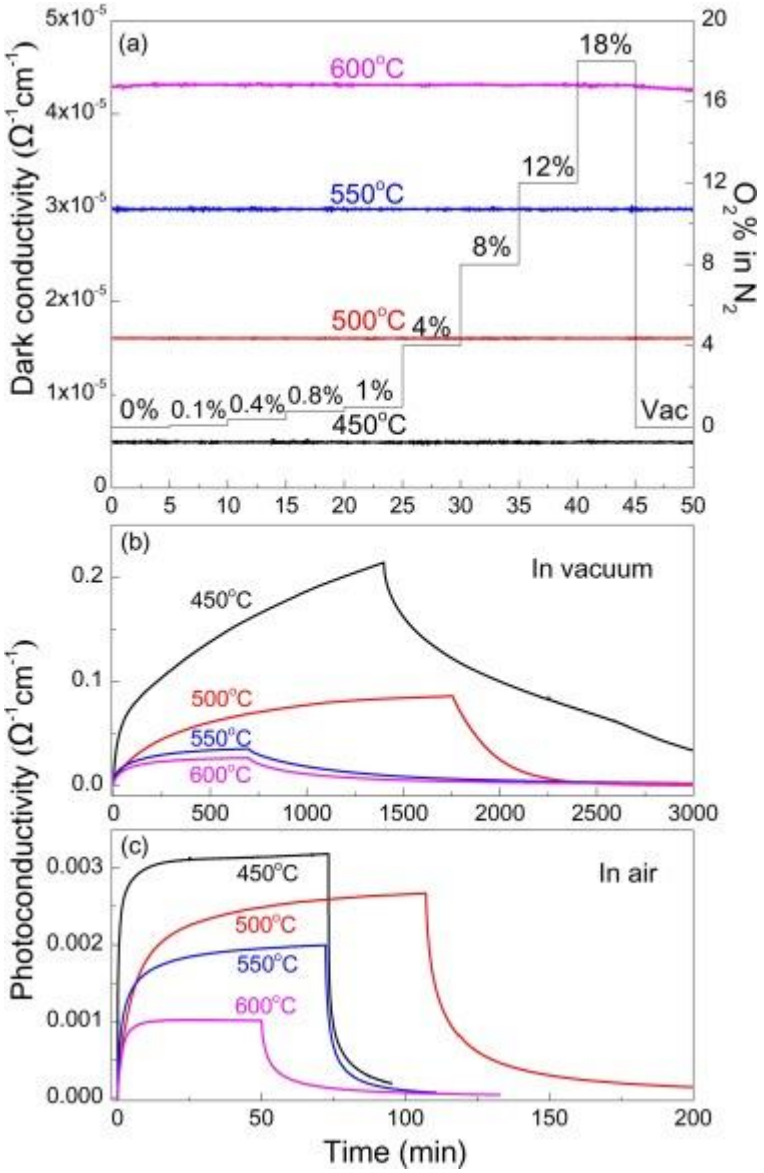

Fig. 4. (a) Room-temperature dark electrical conductivity of SCBD ZnO films post-oxidized at 450 °C to 600 °C in 0–18% O_2-N_2 and vacuum; (b) and (c) room-temperature photoconductivity of the films measured in vacuum and air, respectively.

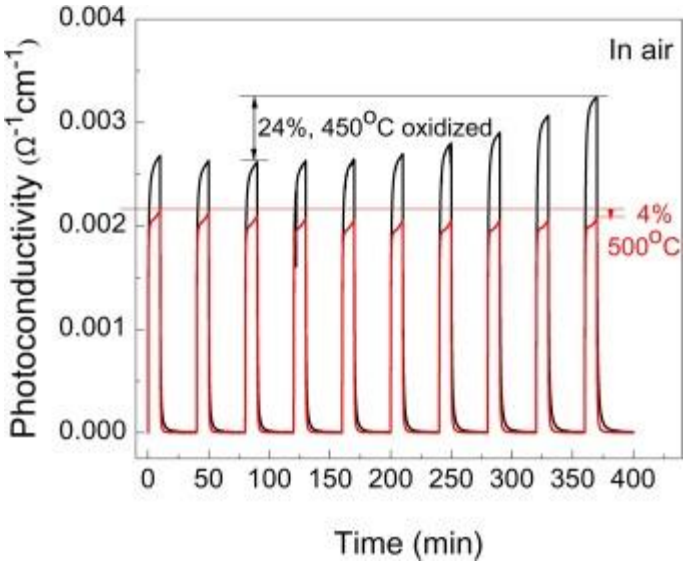

Fig. 5. Room-temperature cyclic photoconductivity of 450 °C and 500 °C post-oxidized SCBD ZnO films measured in air.

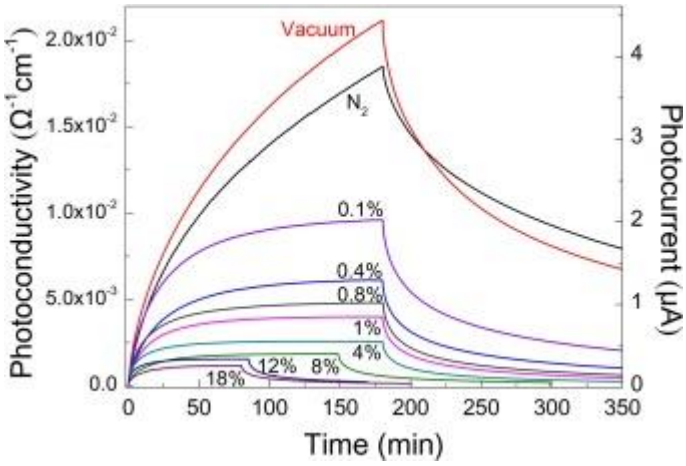

Fig. 6. Room-temperature dynamic photoconductivity and photocurrent of a 500 °C post-oxidized SCBD ZnO film to 0–18% O_2 in N_2 in dry gaseous environment.

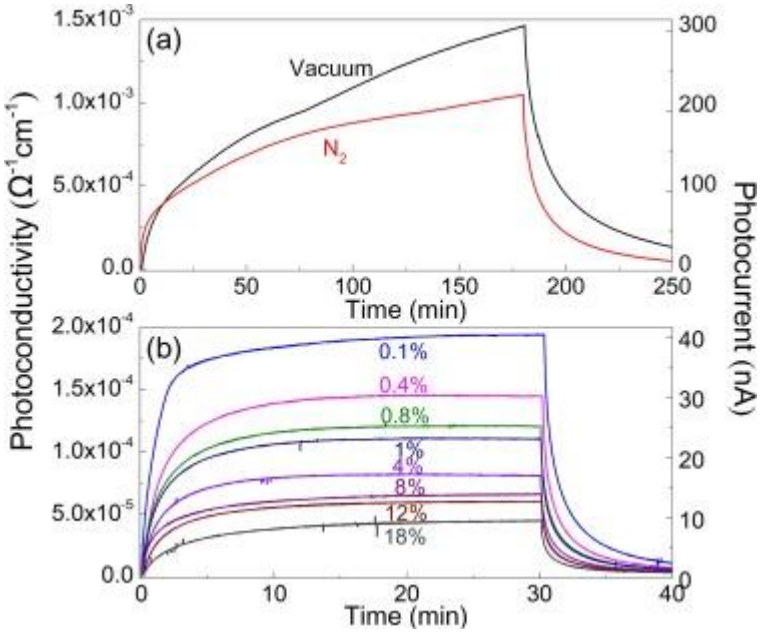

Fig. 7. (a) and (b) Room-temperature dynamic photoconductivity and photocurrent of a polymer-coated 500 °C post-oxidized SCBD ZnO film measured in 0–18% O_2 in dry gaseous environment.

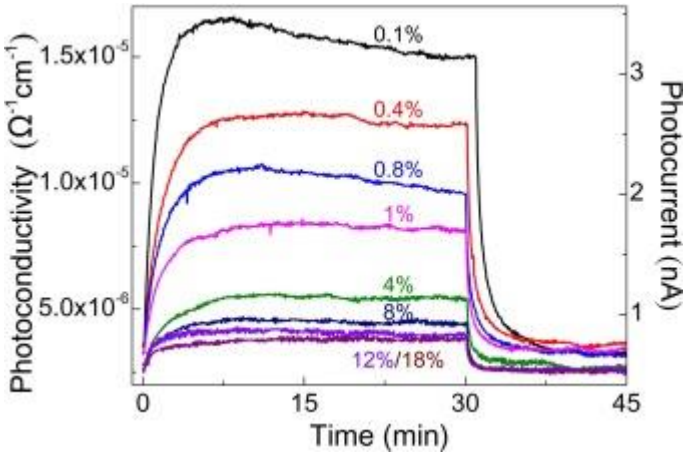

Fig. 8. Room-temperature dynamic photoconductivity and photocurrent of a polymer-coated 500 °C post-oxidized SCBD ZnO film in 0–18% O_2 in 95% humid gaseous environment.

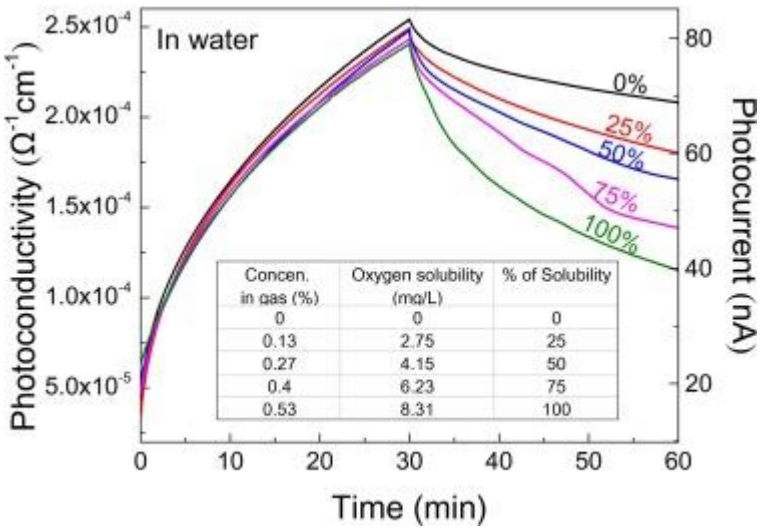

Fig. 9. Room-temperature dynamic photoconductivity and photocurrent of a polymer-coated 500 °C post-oxidized SCBD ZnO film in water with 0–100% dissolved oxygen content.

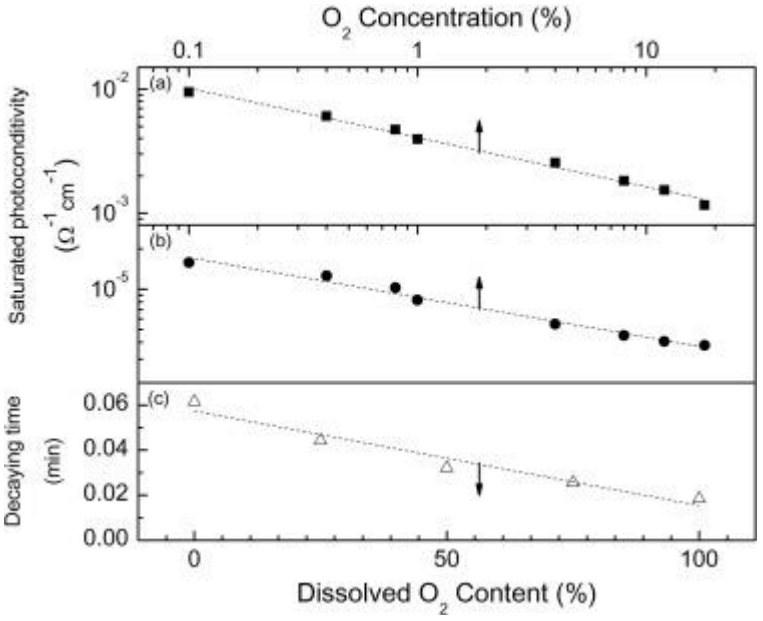

Fig. 10. Three examples of relationships correlating the fitting parameters obtained from the dynamic photocurrent of a 500 °C post-oxidized SCBD ZnO film and O_2 concentration. (a) I_{sat} of an uncoated film versus O_2 concentration in dry O_2-N_2 mixture; (b) I_{sat} of a polymer-coated film versus O_2 concentration in 95% humid O_2-N_2 mixture; and (c) decay time of photocurrent after turning off UV light versus dissolved oxygen content in water.